Crystal growth and its morphology in the mushy zone

doi: 10.1016/j.actamat.2003.11.033

Submitted to ***Acta Materialia***

CRYSTAL GROWTH AND ITS MORPHOLOGY IN THE MUSHY ZONE

H. Yoshioka [a,] *, Y. Tada [b], Y. Hayashi [c]

[a] *Department of Maritime Technology, Toyama National College of Maritime Technology, 1-2 Ebie Neriya, Shinminato-shi, Toyama 933-0293, JAPAN*

[b] *Department of Human and Mechanical Systems Engineering , Kanazawa University, 2-40-20 Kodatsuno, Kanazawa-shi, Ishikawa 920-8667, JAPAN*

[c] *Kanazawa University, Kakuma, Kanazawa-shi, Ishikawa 920-1192, JAPAN*

Keywords : Solidification; Alloys; Microstructure; Crystal growth; Mushy zone

Hideaki Yoshioka* (Associate Professor)

Tel.: +81-766-86-5235; fax: +81-766-86-5110.

E-mail address: yoshi@toyama-cmt.ac.jp (H. Yoshioka)

Yukio Tada (Associate Professor)

Tel.: +81-76-234-4740; fax: +81-76-234-4743.

E-mail address: tada@t.kanazawa-u.ac.jp

Yujiro Hayashi (President)

* Author to whom all correspondence should be addressed

Abstract

In the solidification of multicomponent alloys, a mushy zone appears between the solid and liquid regions and promotes stable solidification by accepting the rejected solute regionally. In this study, the link between heat transfer and microstructures of the mushy zone has been studied experimentally and theoretically. First, the crystal morphology of the mushy zone at a microscale was observed by using succinonitrile-acetone solution and Bi-Sn alloys melts. It was found that the mushy zone consists of a leading front, in which the microstructures originate, and a growing region, where solidification proceeds with the fattening of the crystals. Next, the mechanism of dendritic sidebranch evolution was studied, taking into account the interfacial instability. To summarize these results, a macro-microscopic model is presented, and the change of crystal morphology at the microscale level was analyzed in relation to cooling rate, initial concentration, and distance from a cold wall.

NOMENCLATURE

C : solute concentration, wt%

c_p : specific heat, J/kgK

D : solute diffusivity, m^2/s

f : solid fraction

G : temperature gradient, K/m

h : overall heat-transfer coefficient, W/m^2K

K : curvature, m^{-1}

L_H : latent heat of fusion, J/kg

l_C : length of leading front, m, μm

l_2^* : length between crystal tip and instability position, m, μm

m : slope of liquidus line, K/wt%

R : tip radius of crystal, m

Rc : local cooling rate, K/s

r : space coordinate in radial direction, m, mm

T : temperature, K

t : time, s

v : crystal growth velocity, m/s

z : space coordinate in z-direction, m, mm

ΔT_C^* : constitutional supercooling, K

ΔT_K^* : curvature supercooling, K

δ : interfacial thickness, m

δc : concentration boundary-layer thickness, m

ϕ : space coordinate in rotational direction

γ : solid-liquid interfacial energy, J/m^2

Γ : Gibbs-Thomson parameter ($=\gamma T'/\rho L_H$), mK

η : arm spacing, m, μm

κ : distribution coefficient

λ : thermal conductivity, W/mK

ρ : density, kg/m^3

σ^* : stability constant

Sub/Superscripts

$'$: equilibrium/liquidus

$*$: interface

1, 2 : primary, secondary

c : critical

e : eutectic

i : initial

l, *s*, *m* : liquid, solid, mush

w : cold wall

1. INTRODUCTION

Solidification is the restriction of the rotational motion of liquid molecules and results in the solid phase, which consists of a regular or dense assembly of atoms. This is one of the representative transport phenomena, which include fluid flow, heat transfer and mass transfer. Heat transfer sets up a macroscopic temperature field with the acceptance of rejected heat to control the solidification process. The discipline of transport phenomena describes these diffusion processes by virtue of the gradient law on such statically averaged state quantities as temperature and concentration. Thus, the phenomenological approach is useful and powerful for understanding the macroscopic phenomena. In material processing, however, the fixation of structure and composition is the principal objective. During the solidification process of alloys, compositional partitioning occurs, which results in an inhomogeneous solid phase in structure and composition. A dendrite structure, which appears in casting or welding, is a representative inhomogeneity, and its fineness influences the mechanical properties. Therefore, the necessity for developing microscopic modeling without losing the macroscopic viewpoint is emphasized.

In the solidification of alloys, the redistribution of solute due to the difference in solubility between the liquid and solid phases results in some characteristic phenomena. The solute rejected from the solid-liquid interface develops a concentration boundary layer in the liquid near the interface and causes a lowering of the liquidus temperature and constitutional supercooling. This thermodynamically unstable state creates a rough solid-liquid interface, resulting in a cellular- or dendritic-type mushy zone. That is, the mushy zone lies between the solid and liquid zones, and promotes stable solidification by accepting the rejected solute and heat over a range of temperatures. Therefore, in order to discuss the microscopic structure and composition of the solidified material, it is important to clarify the formation process of the mushy zone in which the microstructures originate. With this objective, the development of a microscopic solidification model is essential.

In past studies, conductive heat transfer problems with solidification have been solved by macroscopic analyses in which the timewise and spacewise changes of the solid fraction are incorporated into the energy equation. For example, Tien et al. [1], Cho et al. [2] and Kim et al. [3] reported a solidification analysis using the solid fraction as a function of temperature or position. Braga et al. [4] analyzed the temperature distribution during solidification by using the local solid fraction determined from the phase diagram and the lever rule. The above treatments are used properly, considering the type and property of the alloy. However, the crystal morphology in the mushy zone was not determined and solidification phenomena were macroscopically handled. Studies of the microstructures of cellular and dendritic crystals, which are formed in a steady state solidification process, have focused mainly on directional solidification. Kurz and Fisher [5] studied dendrite growth using a simplified solution for the wavelength of instability, and obtained a relationship between growth conditions and crystal morphology. The relationships between growth conditions and primary arm spacing were analyzed by Okamoto et al. [6], Hunt [7], Trivedi [8] and Kurz et al. [5]. In their research, primary arm spacing is expressed as a function of temperature gradient G and growth velocity v or cooling rate Rc ($=vG$). Regarding the secondary arm spacing, several papers [9,10] indicated a scaling law between secondary arm spacing and crystal tip radius, though the detailed mechanism is not well understood. Regarding the coarsening of secondary arms at a constant temperature, one of the representative theoretical models is given by Kattamis et al. [11]. Microsegregation is also a significant problem in metallic alloy systems, though it does not always affect the physical properties of the product. Shin et al. [12] proposed a microsegregation model which includes the effects of both back-diffusion and coarsening. This surge of research activity has brought significant findings. However, there are large gaps in the level of discussion of crystal morphology and heat transfer.

The objective of this study was to establish a self-consistent solidification model which linked microstructure and macro heat transfer. In the experiment, crystal growth and its morphology were observed by using succinonitrile-acetone solutions and Bi-Sn alloy melts. The mechanism

of sidebranch evolution in the mushy zone was also analyzed, taking into account the interfacial instability due to constitutional supercooling and the depression of the liquidus temperature due to the increment of the curvature. Based on these results, a macro-microscopic analysis for describing the microstructures has been developed.

2. EXPERIMENT

The solidification experiments were conducted using a multicomponent system for the observation of crystal growth and crystal morphology in the mushy zone. Figure 1 shows a schematic of the experimental apparatus. Some aspects of the mushy zone under conditions of directional cooling were observed with a CCD camera installed on a microscope. Samples of succinonitrile-acetone solutions were introduced into a rectangular test cell with inner dimensions 18 mm in length, 8 mm in width, and 1 mm in thickness. The top and bottom walls of the test cell were made of coverglasses in order to allow visualization. A bakelite spacer of 1-mm thickness was sandwiched between the two coverglasses. A cold wall made of an aluminum plate was cooled using a Peltier module. The cooling rate at the cold wall was controlled by regulating the electric current to the module. The temperature distribution inside the test cell was measured using six T-type thermocouples of 0.2-mm diameter. The thermocouples were embedded into the test cell at 2-mm intervals from the cold wall.

Solidification experiments using Bi-Sn alloys were also performed. After directional solidification, samples were submerged in a water tank to quench the solid-liquid interface during solidification. After quenching, the microstructures were observed using a scanning electron microscope.

3. HEAT TRANSFER AND MICROSOLIDIFICATION

Figure 2 shows microstructures of the mushy zone advancing from the cold wall. In this figure, z is the distance from the cold wall to the front of the mushy zone. The mushy zone consists of a large number of dendritic crystals which have a principal axis (primary arm) almost perpendicular to the wall and four side-branches (secondary arms) around the circumference of the axis. These crystals grow in the direction opposite to the heat flow. It is also found that the primary arm spacing decreases with increasing distance from the cold wall, because the local cooling rate decreases. A close-up of the observed mushy zone is shown schematically in Fig. 3. It is convenient to think that the mushy zone consists of a leading front and a growing region. At the leading front, the equally spaced secondary arms grow with the development of the concentration boundary layer, and the microstructures originate in this place. In the growing region, the growth of the secondary arms almost stops due to the interaction of the concentration boundary layer, and the fattening of the crystal arm proceeds.

Figure 4 shows the microsolidification process in relation to heat transfer. Solidification of the multicomponent alloys advances with the mushy zone between the solid and liquid phase. Thus, by using heat conduction equations (including the heat generation term due to solidification), the temperature, interface position, local cooling rate, and crystal growth velocity are obtained at a macroscale. At a microscale, the microstructural characteristics, including tip radius, primary arm spacing and secondary arm spacing, originate at the leading front, and solidification proceeds by the fattening of crystals in the growing region. At the same time, coarsening of the crystal also occurs as each small branch is expelled by a big branch. Finally, the solidified texture is almost fixed under eutectic composition, and it changes with time by back-diffusion. The solidification having these micro behaviors can be analyzed in relation to the macro heat transfer. In macro analysis, the region of the leading front is neglected because of its small dimension. Therefore, microsolidification can be analyzed on the basis of local state variables calculated from macro heat-transfer analysis.

4. CRYSTAL GROWTH AND ITS MORPHOLOGY AT THE LEADING FRONT

The geometrical shape of the leading front is characterized by the radius of curvature of the crystal tip R and the primary arm spacing η_1. The secondary arm spacing η_2 influences the internal structure. In this section, these microstructural characteristics of a crystal are discussed in relation to the macroscopic state quantities at the leading front.

4.1. Tip shape of crystal (radius of curvature)

The growth velocity of a crystal due to heat conduction v is defined as the velocity that the field temperature T crosses the liquidus temperature at the initial concentration $T'(C_i)$. A slight supercooling at the crystal tip is necessary to drive crystal growth, and the supercooling correlates to the stable configuration of a tip having critical interfacial energy. The crystal tip radius R can be approximately expressed by the stability criterion of Kurz and Fisher [5] as follows:

[low v-range]

$$R = \frac{2D}{(1-\kappa)v} + \frac{2mC_i}{G} \qquad \text{for} \quad v < v_{tr}\,, \tag{4.1}$$

[high v-range]

$$R = \left(\frac{D\Gamma}{-m(1-\kappa)C_i \sigma^* v} \right)^{1/2} \qquad \text{for} \quad v > v_{tr}\,, \tag{4.2}$$

where v_{tr} (=$-GD/mC_i(1-\kappa)$) is the transition rate from a low- to high-velocity regime, and σ^* is a stability constant (=$1/4\pi^2$: by planar interface model [13]). In this study, the experimentally measured velocity range corresponds to the high v-range because the maximum value of v_{tr} is 0.3 μm/s. Figure 5 shows the tip radius as a function of the growth velocity of the crystal. The analytical results almost agree with the experimental results. Therefore, it is possible to apply Kurz and Fisher's model for the crystal tip radius.

4.2. Primary arm spacing

Figure 6(a) shows the change of primary arm spacing η_1 with local cooling rate *Rc* at the leading front. Here, *t* is the time after the solidification starts at a wall surface. *Rc* decreases exponentially with time. Corresponding to this, η_1 increases with time and soon becomes almost constant. Figure 6(b) shows η_1 as a function of *Rc*. The primary arm spacing becomes smaller when the solute concentration is smaller and the local cooling rate is larger. It seems that solute diffusion during the solidification process sets the primary arm spacing as the framework of structures of the mushy zone. Okamoto and Kishitake [6] assumed that η_1 is equal to the thickness of the solute diffusion layer from the interface during solidification, and obtained the following equation:

$$\eta_1 = 2\beta\left(\frac{-m(1-\kappa)C_i D}{Rc}\right)^{1/2}, \tag{4.3}$$

where β is the correction factor due to effect of the crystal shape, and *m* is the slope of the liquidus line. The straight line in Fig. 6(b) represents the analytical results calculated from Eq. (4.3), assuming the cooling rate is defined as the value at the tip of the crystal. Here, β=0.25 was employed for the dendritic interface in order to fit the theoretical lines to experimental data, and β=0.125 was employed for the cellular interface. Good agreement between the theoretical and experimental results shows that the theory of Okamoto et al. can be applied at the leading front.

4.3. Secondary arm spacing

The generation of the secondary arms is investigated, taking into account surface instability due to constitutional supercooling. Figure 7 shows the mechanism of interfacial instability. Since the seed of a secondary arm is fixed one after another at its germination point, secondary arm spacing η_2 depends on the growth velocity of the primary arm *v* and instability cycle t_c:

$$\eta_2 = v \cdot t_c . \tag{4.4}$$

Since the concentration boundary layer develops around the primary arm surface, constitutional supercooling occurs and brings about the seed of surface instability. The temperature and solute concentration near the primary arm surface are shown in Fig. 7. Temperature is expressed as the uniform temperature T since, in general, the thermal diffusivity of alloys is several orders of magnitude greater than the mass diffusivity. The solute concentration is replaced by the liquidus temperature T' instead of the concentration. The constitutional supercooling, $\Delta T_c = T' - T$, due to the difference between the diffusion velocity of heat and diffusion velocity of solute, promotes the interfacial instability, but the effect of curvature/interfacial energy favors stable growth of the interface. Hence, the instability criterion is decided by the competition of both factors.

As shown in Fig. 7, the perturbation on the surface of the primary arm is assumed. The perturbation having the prior wave number k in the circumferential direction ϕ and the frequency ω in the growth direction z is expressed as [14]:

$$\rho(\phi, z, t) = \delta(t) + \varepsilon \cos(k\phi)\cos(\omega z), \tag{4.5}$$

where δ is the radius of the primary arm, and ε is the minute amplitude. For the succinonitrile-acetone solution considered here, the number of sidebranches in the circumference is four due to the crystal anisotropy, as shown in Figs. 2 and 3. The instability period is assumed to be equal to the secondary arm spacing. Therefore,

$$k = 4, \ \omega = 2\pi / \eta_2 \tag{4.6}$$

is given. The curvature of the interface when a perturbation occurs is described by:

$$K = \frac{1}{\delta} + \frac{\varepsilon}{\delta^2}\left\{k^2 + (\delta\omega)^2 - 1\right\}. \tag{4.7}$$

Thus, the increment of the interface curvature due to perturbation is expressed by:

$$\Delta K = \frac{\varepsilon}{\delta^2}\left\{k^2 + (\delta\omega)^2 - 1\right\}. \tag{4.8}$$

By using Gibbs-Thomson's relationship, the reduction of the equilibrium liquidus temperature due to the curvature increment is given by the following equation:

$$\Delta T_K^* = \Gamma \Delta K, \tag{4.9}$$

where Γ is Gibbs-Thomson's coefficient. Fick's equation for rejection/diffusion of solute at the interface is expressed by:

$$\left(\frac{\partial C}{\partial r}\right)_\delta = -\frac{(1-\kappa)C_l'(T^*)}{D}\frac{d\delta}{dt}, \tag{4.10}$$

where C_l' is the equilibrium relationship between temperature and concentration, represented by the liquidus line. Considering that the width of the leading front is extremely small, the interface temperature T^* can be approximately represented as:

$$T^* \approx T'(C_i). \tag{4.11}$$

Under these conditions, the constitutional supercooling at the tip of a perturbation is expressed as:

$$\Delta T_C^* = m\left(\frac{\partial C}{\partial r}\right)_\delta \varepsilon. \tag{4.12}$$

Therefore, the critical condition of interface instability is given by:

$$\Delta T_C^* - \Delta T_K^* \geq 0. \tag{4.13}$$

Namely, when ΔT_C^* becomes larger than ΔT_K^*, the perturbation amplifies and a secondary arm is formed.

In the calculation, two types of shapes for the crystal tip were considered, as shown in Table 1. For the parabolic shape, assuming that the time required for the interface to attain the unstable state is equal to the instability cycle t_c, the critical interfacial thickness for instability of the primary arm is given by:

$$\delta(t_c) = \sqrt{2R\eta_2}\,. \tag{4.14}$$

And the crystal fattening velocity is given by:

$$\left|\frac{d\delta}{dt}\right|_{t=t_c} = \sqrt{\frac{Rv^2}{2\eta_2}}\,, \tag{4.15}$$

so that the rates of change of v and R with time are small enough to disregard.

Finally, substituting Eqs. (4.8)-(4.12), (4.14) and (4.15) in Eq. (4.13) yields:

$$\frac{-m(1-\kappa)C_i v}{D}\sqrt{\frac{R}{2\eta_2}} - \Gamma\left\{\frac{k^2-1}{2R\eta_2} + (2\pi/\eta_2)^2\right\} = 0\,. \tag{4.16}$$

Likewise, for the catenary shape, we obtained:

$$\frac{-m(1-\kappa)C_i v}{D\sqrt{(\eta_2/R)(\eta_2/R+2)}} - \Gamma$$
$$\times \left[(k^2-1) \Big/ \left\{ R\cosh^{-1}(\eta_2/R+1) \right\}^2 + (2\pi/\eta_2)^2 \right] = 0. \qquad (4.17)$$

By using the experimentally determined growth velocity, η_2 can be calculated from Eqs. (4.2), (4.16) or (4.17).

Figure 8 shows η_2 as a function of crystal growth velocity. It is found that η_2 decreases with increasing growth velocity or increasing initial concentration. The reason is that the instability cycle t_c is reduced by lowering the solute rejection rate due to the increase in *v,* and by raising the rejected solute amount due to the increase in C_i. Comparing the case of the parabolic shape with the catenary one, the catenary shape agrees well with experimental values. Although the parabolic shape is a solution for the steady state single-growth model [15], a comparatively thin catenary shape seems to be more suitable for the array growth, since interference between the neighboring crystals would occur in terms of the rejected solute and latent heat. Although there was some simplified modeling, such as cylindrical perturbation for the crystal surface which actually has some curvatures in *z*-direction, the analytical results agree with the experimental results enough to indicate the validity of this model. Moreover, by rearranging ξ (=η_2/R) by substituting Eq. (4.2) in Eq. (4.17), the following equation is obtained:

$$\left\{ \xi\cosh^{-1}(\xi+1) \right\}^2 - \sigma^* \sqrt{\xi(\xi+2)}$$
$$\times \left[(k^2-1)\xi^2 + \left\{ 2\pi\cosh^{-1}(\xi+1) \right\}^2 \right] = 0. \qquad (4.18)$$

The solution of the above equation is ξ=2.13, and it fulfills the scaling law between *R* and η_2. This doesn't conflict with the experimental report of Trivedi [10].

5. HEAT TRANSFER MODEL

Heat transfer during the solidification of multicomponent materials is developed in three regions: a liquid zone ($n=l$), a mushy zone ($n=m$) and a solid zone ($n=s$). For determining the macroscopic heat transfer, the basic equations, and the initial and boundary conditions, are formulated as shown in Table 2 with reference to the physical and coordinate system shown in Fig. 4. Equation (5.1) is a one-dimensional heat conduction equation. The second term on the right side of Eq. (5.2) is the heat generation term that is dependent upon the solid fraction. We used the expression of Eq. (5.2) as apparent thermal diffusivity that includes the latent heat effect in the heat capacity. Although f in Eq. (5.2) is the volume solid fraction, replacing this with solid mass fraction may be similar. Equation (5.4) is Sheil's equation [16], which provides the relationship between the temperature and solid mass fraction in the mushy zone. Equation (5.7) is a boundary condition for the uniform, overall heat-transfer coefficient at the cold wall. The locations of liquid-mushy interface ζ_m and mushy-solid interface ζ_s are provided in Eqs. (5.8) and (5.9). Equation (5.10) describes the advance of the eutectic solid. The thermal properties in the mushy zone, χ ($=\rho, c_p, \lambda$), are weight-averaged according to the local solid fraction as follows:

$$\chi_m = \chi_s f + \chi_l (1 - f). \tag{5.11}$$

6. MACRO-MICROSCOPIC ANALYSIS

On the basis of the connection of heat transfer and microsolidification shown in Fig. 4, numerical simulations were carried out.

6.1. Analytical model

The equations for determining the microstructural characteristics are represented in Table 3. For heat transfer in solidification with a mushy zone, solving Eq. (5.1) with the heat generation term due to solidification describes these macroscopic fields: temperature T, solid fraction f, and interface location ζ. Primary arm spacing η_1 and tip radius R are calculated from Eqs. (4.3) and (4.2) by using the local state variables (Rc, v) at the leading front. Initial secondary arm spacing η_2 is given by solving the unstable field produced in the flank of the primary arm in Eq. (4.17).

The cellular-to-dendrite transition is explained under the physical and coordinate system shown in Fig. 9. Here, l_2^* is the length between the crystal tip and the instability position determined from Eq. (4.17) as $l_2^*=\eta_2$, and l_c is the length of the leading front which is defined as the distance between the crystal tip and the position at which the adjacent concentration boundary layers interact. The constitutional supercooling which promotes the growth of secondary arms would gradually vanish after the concentration boundary layer fully develops. Therefore, for the case in which the instability generation position is out of the leading front, that is, l_2^* is larger than l_c, the perturbation on the surface does not amplify, so a cellular crystal forms. For the case in which l_2^* is smaller than l_c, secondary arms develop, so a dendritic crystal forms in the leading front. The concentration distribution in the liquid phase ,C_l, was approximated by the secondary curve of Eq. (6.1), and solved by using the profile method under the boundary conditions of Eqs. (6.2)-(6.4). Equation (6.5) provides the mass balance in the radial direction of the crystal. The concentration boundary layer thickness δc can be calculated from Eq. (6.5), receiving the interfacial thickness δ. The length of the leading front is calculated from Eq. (6.6), since it is given by the product in the crystal growth velocity and the time required for δc to attain half of η_1 in the r direction. Finally, the criterion of the cellular-to-dendrite transition is described by Eq. (6.7).

6.2. Simulations

A numerical simulation was carried out for the succinonitrile-acetone solution. The initial

condition is set with the temperature at the time when the wall surface temperature T_w descends to the liquidus temperature $T'(C_i)$. The boundary condition is given by Eq. (5.7), where $Ta=T'(C_i)$-60 K, h=100 W/m^{2}K. The calculation for Eq. (5.1) was carried out by using the forward difference method with conditions of Δz=0.1 mm, Δt=0.01 s. The main thermophysical properties were obtained from the literature [9]. Furthermore, considering that the thermal diffusivity of glass used as the solidification cell is comparatively large, the calculated results were revised by using the thermophysical properties averaged according to the volume ratio of the cell and the sample, that is, 1:5.

The predicted results for two samples of different concentrations are shown in Fig. 10: Fig. 10(a) shows the change of temperature and solid fraction with time, and Fig. 10(b) shows the microstructural characteristics (η_1, η_2). The timewise evolution of macroscopic fields such as temperature, solid fraction and interface location can be obtained as shown in Fig. 10(a). The solid fraction in the case of the higher initial concentration is smaller compared to the case of the lower initial concentration. This is caused by the difference of the solute amount rejected from the interface. Namely, in the case of the higher initial concentration, a significant lowering of the liquidus temperature appears due to the larger rejected solute. The timewise change of the temperature in Fig. 10(a) determines the local state variables at the leading front (Rc, v). Utilizing the spacewise changes of these local state variables, the microstructural characteristics were predicted, as shown in Fig. 10(b). Primary arm spacing η_1 increases from approximately 80 μm to 200 μm, and becomes almost uniform. This fact corresponds with the decrease in local cooling rate Rc away from the cold wall. Secondary arm spacing η_2, which is generated on the flank of the primary arm, increases from approximately 30 μm to 50 μm, with the decrease in the crystal growth velocity v. Due to the dependence of microstructural characteristics on solute concentration, η_1 increases with increasing C_i. This is because the concentration boundary layer developes. η_2 decreases with increasing C_i, since the concentration boundary layer is easy to shift to an unstable state.

Next, for the Bi-Sn alloy system, an analysis was carried out where the spacewise change of the crystal morphology was simply analyzed by using the local state variables measured experimentally. Among the thermophysical properties used in the calculation, the solute diffusivity is D=1.43x10^{-9} m^2/s (at approximately 250 ˚C) [17].

A comparison of the experimental and analytical results for the cellular-to-dendrite transition is shown in Fig. 11. In the case of Sn-10wt%Bi, shown by the circles, the crystal morphology changes from cells to dendrites at about the 8-mm position. Corresponding to this, in the calculation, l_c becomes larger than l_2^* from the 7.2-mm position. In the case of the faster cooling rate at the same solute concentration, the cellular-to-dendrite transition point becomes closer to the cold wall. In the case of Sn-30wt%Bi, the dendritic structure is formed everywhere since the interface becomes quickly unstable due to constitutional supercooling. Good agreement between experimental and analytical results suggests the validity of this treatment for the morphology transition.

7. CONCLUSIONS

In the solidification of multicomponent systems, crystal growth and its morphology in the mushy zone was investigated. The following conclusions were obtained:

1. The mushy zone consists of the leading front and the growing region. At the leading front, the microstructural characteristics, including tip radius, primary arm spacing and secondary arm spacing, originate. In the growing region, solidification proceeds by the fattening of the crystal.
2. The tip radius depends on the crystal growth velocity, and obeys the Kurz and Fisher's model.
3. Considering primary arm spacing, there is a difference between dendritic and cellular crystals, but in both the arm spacing is inversely related to the square root of the local cooling rate at the leading front. The theory of Okamoto et al. can be applied at the leading front.
4. The mechanism of sidebranch evolution is clarified on the basis of the interfacial instability

theory, and secondary arm spacing is expressed as a function of crystal growth velocity and initial solute concentration.

5. On the basis of these results, the macro-microscopic solidification model has been presented to predict the microstructures: the primary, the secondary arm spacing, and the morphology of the cell or dendrite. The validity of the model presented is made clear by comparing with experimental results.

REFERENCES

[1] Tien RH, Geiger GE. ASME J Heat Transfer 1967;89:230.

[2] Cho SH, Sunderland JE. Trans ASME, J Heat Transfer 1969;91:421.

[3] Kim CJ, Kaviany M. Int J Heat Mass Transfer 1992;35:1143.

[4] Braga SL, Viskanta R. Int J Heat Mass Transfer 1990;33:745.

[5] Kurz W, Fisher DJ. Acta Metall 1981;29:11.

[6] Okamoto T, Kishimoto K. J Cryst Growth 1975;29:137.

[7] Hunt JD. Mater Sci Eng 1984;65:75.

[8] Trivedi R. Metall Trans 1984;15A:977.

[9] Somboonsuk K, Mason JT, Trivedi R. Metall Trans 1984;15A:967.

[10] Trivedi R, Somboonsuk K. Mater Sci Eng 1984;65:65.

[11] Kattamis TZ, Coughlin JC, Flemings MC. Trans Met Soc AIME 1967;239:1504.

[12] Shin YH, Kim MS, Oh KS, Yoon EP, Hong CP. ISIJ International 2001;41:158.

[13] Langer JS, Müller-Krumbhaar H. Acta Metall 1978;26:1681.

[14] Hardy SC, Coriell SR. J Cryst Growth 3 1968;4:569.

[15] Ivantsov GP. Dokl Akad Nauk USSR 1947;58:567.

[16] Sheil E. Z Metllkd 1942;34:70.

[17] Niwa K, Kado S, Nakajima H, Ichikawa K. J Japan Inst Metals 1964;28:353.

Table Captions

Table 1

Tip shape

Table 2

The basic equation, initial and boundary conditions for determining the one-dimensional macroscopic heat transfer

Table 3

Equations for determining the microstructural characteristics

Table 1 Tip shape

parabolic shape	catenary shape
$\delta(t) = \sqrt{2Rvt}$	$\delta(t) = R \cosh^{-1}\left(\frac{vt}{R} + 1\right)$
$\frac{d\delta}{dt} = \sqrt{\frac{Rv}{2t}}$	$\frac{d\delta}{dt} = \frac{v}{\sqrt{(vt/R)\,(vt/R + 2)}}$

Table 2 The basic equation, initial and boundary conditions for determining the one-dimensional macroscopic heat transfer

Basic Equations

$$\frac{\partial T_n}{\partial t} = \alpha_n \frac{\partial^2 T_n}{\partial z^2} \tag{5.1}$$

$$\alpha_n = \lambda_n / \left\{ (\rho c_p)_n - \rho_l L_H \frac{\partial f_n}{\partial T_n} \right\} \tag{5.2}$$

Solid Fraction

$$f_l = 0 \tag{5.3}$$

$$f_m = 1 - \left(\frac{C_l'(T)}{C_i} \right)^{1/(\kappa - 1)} \tag{5.4}$$

$$f_s = 1 \tag{5.5}$$

I.C. & B.C.

$$T_n(z,0) = T_i \tag{5.6}$$

$$\lambda_n \left(\frac{\partial T_n}{\partial z} \right)_{z=0} = h\,(T_w - T_a) \tag{5.7}$$

$$T_l(\zeta_m,t) = T_m(\zeta_m,t) = T'(C_i) \tag{5.8}$$

$$T_m(\zeta_s,t) = T_s(\zeta_s,t) = T'(C_e) \tag{5.9}$$

$$\lambda_s \left(\frac{\partial T_s}{\partial z} \right)_{\zeta_s} - \lambda_m \left(\frac{\partial T_m}{\partial z} \right)_{\zeta_s} = \rho L_H (1 - f_e) \frac{d\zeta_s}{\partial t} \tag{5.10}$$

Table 3 Equations for determining the microstructural characteristics

- Macroscopic Heat Transfer (Rc, v, $T(z,t)$)

  Eq. (5.1)

- Microstructure (η_1, R)

  Eqs. (4.3) and (4.2)

- Microstructure (η_2 or l_2^*)

  Eq. (4.17)

- Criterion for Cellular-to-Dendrite Transition

$$C_l(r,t) = ar^2 + br + c \tag{6.1}$$

$$\frac{dC_l}{dr} \approx -\frac{C_i(1-\kappa)}{D}\frac{d\delta}{dt} \quad \text{at } r = \delta \tag{6.2}$$

$$\frac{dC_l}{dr} = 0 \quad \text{at } r = \delta c \tag{6.3}$$

$$C_l = C_i \quad \text{at } r = \delta c \tag{6.4}$$

$$2\pi \int_{\delta}^{\delta c} C_l r\, dr \approx \pi(\delta c^2 - \kappa\delta^2)C_i \tag{6.5}$$

$$l_C = vt \quad \text{at } \delta c(t) = \frac{\eta_1}{2} \tag{6.6}$$

$$\left.\begin{array}{l} l_C < l_2^* : \text{Cells} \\ l_C \geq l_2^* : \text{Dendrites} \end{array}\right\} \tag{6.7}$$

Figure Captions

Fig. 1. Apparatus.

Fig. 2. Microstructure of a mushy zone (SCN-5wt%acetone).

Fig. 3. Schematic of dendritic-type mushy zone.

Fig. 4. Link between heat transfer and microsolidification.

Fig. 5. Tip radius of a crystal.

Fig. 6. Primary arm spacing: (a) timewise change of primary arm spacing and local cooling rate; (b) relationship between primary primary arm spacing and local cooling rate.

Fig. 7. Mechanism of interfacial instability.

Fig. 8. Secondary arm spacing.

Fig. 9. Physical-coordinate system (Criterion for cellular-to-dendrite transition).

Fig. 10. Simulation results (SCN-acetone system): (a) macroscopic heat transfer; (b) microstructural characteristics.

Fig. 11. Cellular-to-dendrite transition (Bi-Sn system).

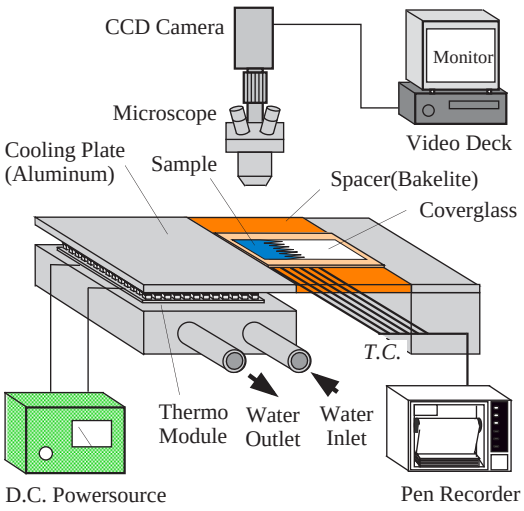

Fig. 1. Apparatus.

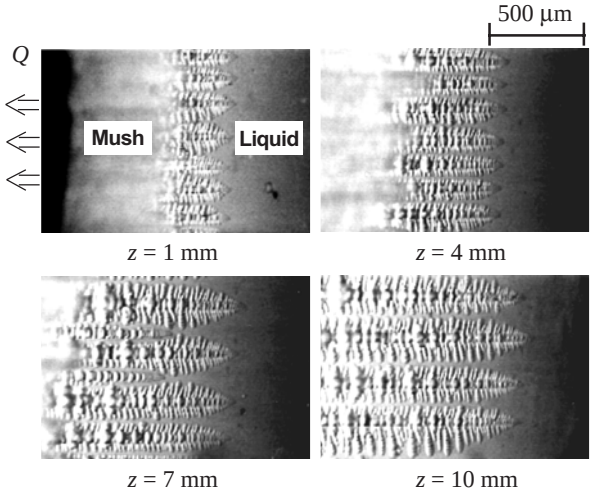

Fig. 2. Microstructure of a mushy zone (SCN-5wt%acetone).

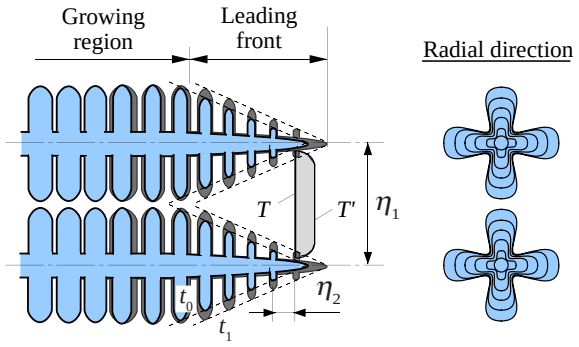

Fig. 3. Schematic of dendritic-type mushy zone.

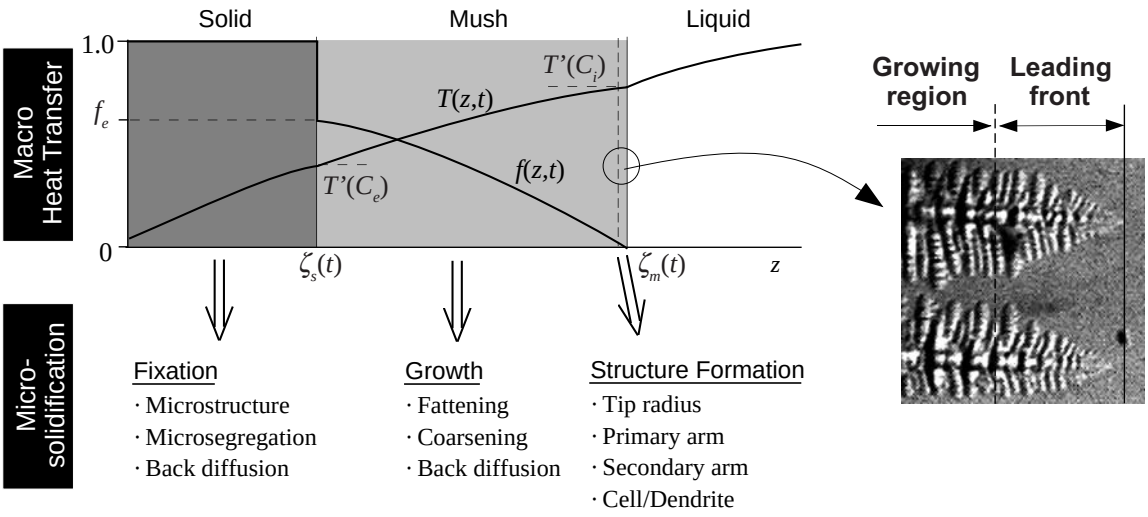

Fig. 4. Link between heat transfer and microsolidification.

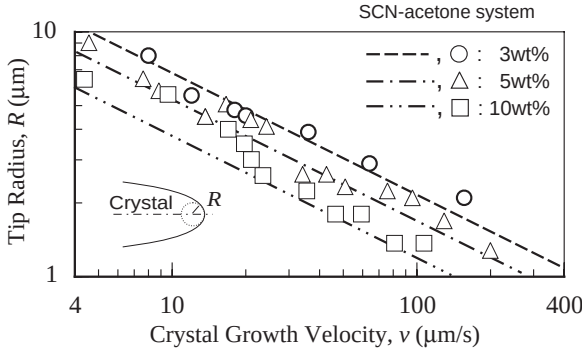

Fig. 5. Tip radius of a crystal.

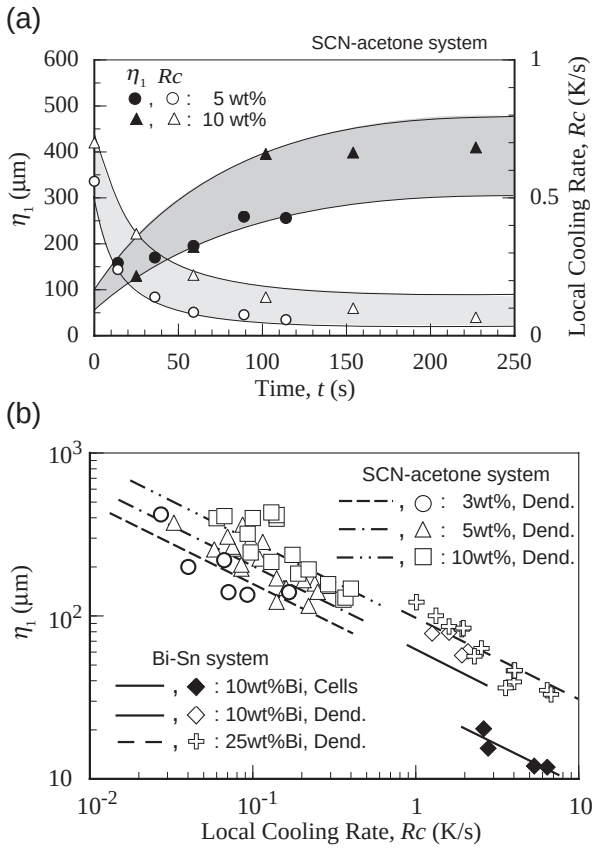

Fig. 6. Primary arm spacing: (a) timewise change of primary arm spacing and local cooling rate; (b) relationship between primary primary arm spacing and local cooling rate.

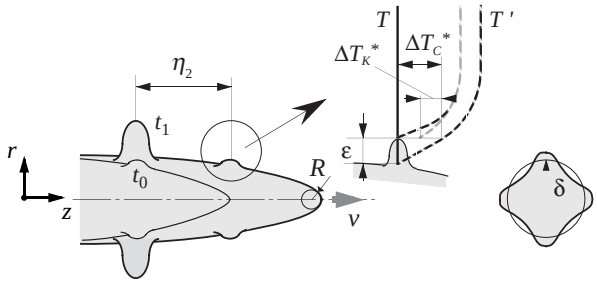

Fig. 7. Mechanism of interfacial instability.

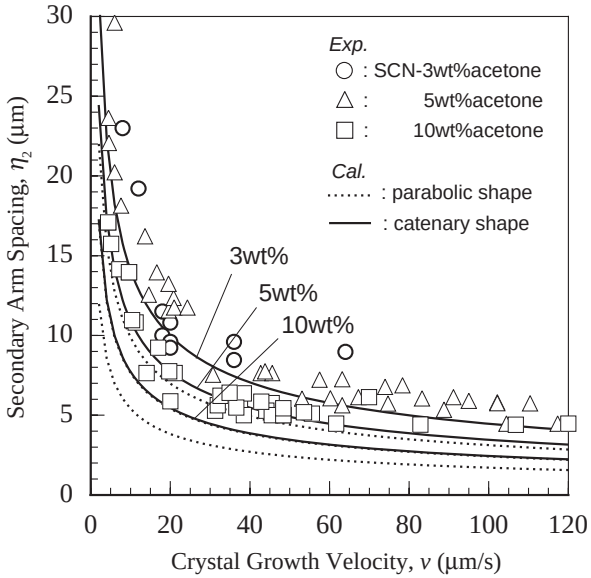

Fig. 8. Secondary arm spacing.

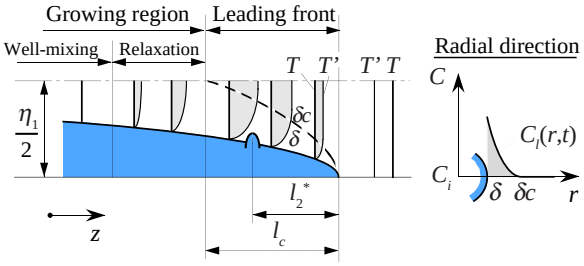

Fig. 9. Physical-coordinate system (Criterion for cellular-to-dendrite transition).

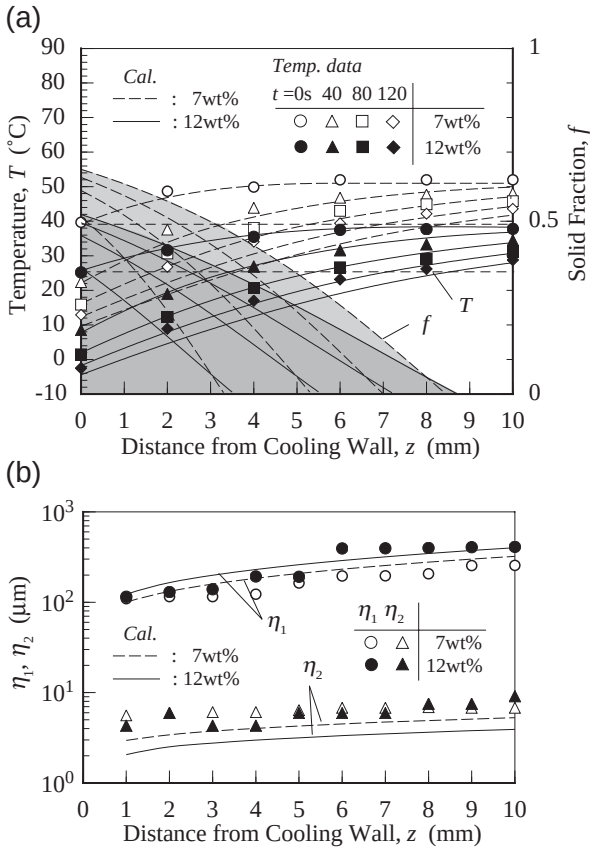

Fig. 10. Simulation results (SCN-acetone system): (a) macroscopic heat transfer; (b) microstructural characteristics.

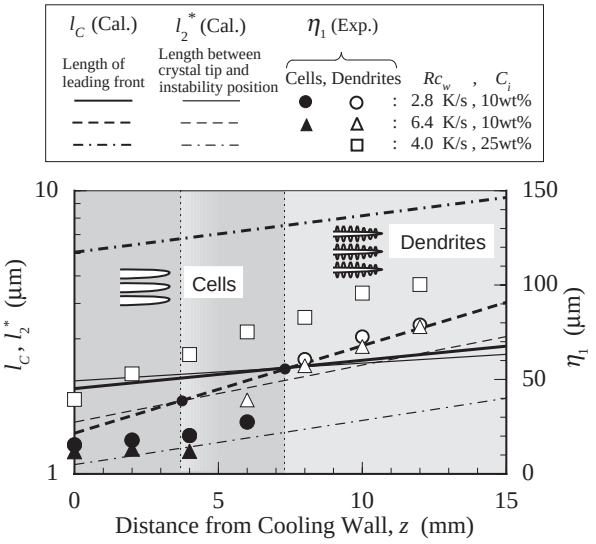

Fig. 11. Cellular-to-dendrite transition (Bi-Sn system).